Neutron background measurements with a hybrid neutron detector at the Kuo-Sheng Reactor Neutrino Laboratory

A. Sonay,[1,2] M. Deniz,[1,2,*] H. T. Wong,[2,*] M. Agartioglu,[1,2] G. Asryan,[2] J. H. Chen,[2] S. Kerman,[1,2] H. B. Li,[2] J. Li,[3] F. K. Lin,[2] S. T. Lin,[2,4] B. Sevda,[1,2] V. Sharma,[2,5] L. Singh,[2,5] M. K. Singh,[2,5] M. K. Singh,[2,5] V. Singh,[5] A. K. Soma,[2,5] S. W. Yang,[2] Q. Yue,[6] I. O. Yıldırım,[7] and M. Zeyrek[7]
(TEXONO Collaboration)
[1]*Department of Physics, Dokuz Eylül University, Buca, İzmir TR35390, Turkey*
[2]*Institute of Physics, Academia Sinica, Taipei 115, Taiwan*
[3]*Institute of High Energy Physics, Chinese Academy of Science, Beijing 100039, China*
[4]*College of Physical Science and Technology, Sichuan University, Chengdu 610064, China*
[5]*Department of Physics, Institute of Science, Banaras Hindu University, Varanasi 221005, India*
[6]*Department of Engineering Physics, Tsinghua University, Beijing 100084, China*
[7]*Department of Physics, Middle East Technical University, Ankara TR06800, Turkey*

(Received 28 March 2018; published 2 August 2018)

We report *in situ* neutron background measurements at the Kuo-Sheng Reactor Neutrino Laboratory (KSNL) by a hybrid neutron detector (HND) with a data size of 33.8 days under shielding configurations identical to those used during the neutrino physics data taking. The HND consists of BC-501A liquid and BC-702 phosphor powder scintillation neutron detectors, which are sensitive to both fast and thermal neutrons, respectively. Neutron-induced events for the two channels are identified and differentiated by pulse shape analysis, such that the backgrounds of both are simultaneously measured. The fast neutron fluxes are derived by an iterative unfolding algorithm. Neutron-induced backgrounds in the germanium detector under the same fluxes, due to both cosmic rays and ambient radioactivity, are derived and compared with the measurements. The results are valuable to background understanding of the neutrino data at the KSNL. In particular, neutron-induced background events due to ambient radioactivity as well as from reactor operation are negligible compared to intrinsic cosmogenic activity and ambient γ activity. The detector concept and analysis procedures are applicable to neutron background characterization in similar rare-event experiments.

DOI: 10.1103/PhysRevC.98.024602

I. INTRODUCTION

The TEXONO Collaboration [1] is pursuing experimental investigation of neutrino physics [2–5], as well as weakly interacting massive particle (WIMP) dark matter [6], axions, [7] and other physics searches beyond the standard model [8] at the Kuo-Sheng Reactor Neutrino Laboratory (KSNL). Quantitative understanding of neutron-induced backgrounds and the nature of their sources is crucial to these studies.

We report in this article *in situ* measurement of thermal ($n_{\rm thermal}$) and fast ($n_{\rm fast}$) neutron backgrounds at the KSNL under shielding configurations identical to those used during the various physics data taking. A custom-built hybrid neutron detector (HND), whose characteristics and performances were reported earlier in our previous publication [9], is used for these measurements.

The paper is structured as follows. Highlights of the KSNL are presented in Sec. II. The unique merits of the HND, its features, and the associated pulse shape discrimination (PSD) techniques are summarized in Sec. III. Data taking at the KSNL is discussed in Sec. IV. Derivation of the internal contamination of the HND is discussed in Sec. V. Results on the measured neutron-induced background in the HND, the calculated neutron fluxes, and the projected background to high-purity germanium detectors (HPGe) at the same location are presented in Sec. VI.

II. THE KUO-SHENG REACTOR NEUTRINO LABORATORY

The Reactor Neutrino Facility at the KSNL [1–3] is located at a distance of 28 m from core 1 of the Kuo-Sheng Nuclear Power Station at the northern shore of Taiwan. The site is on the ground floor of the reactor building at a depth of 10 m below ground level, with an overburden of about 30 meter water equivalence (mwe). The nominal thermal power output is 2.9 GW supplying a $\bar{\nu}_e$ flux of about 6.4×10^{12} cm^{-2} s^{-1}. A schematic view is depicted in Fig. 1(a).

A multipurpose "inner target" detector volume of 100 cm × 80 cm × 75 cm is enclosed by 4π passive shielding materials that have a total weight of about 50 tons. The shielding provides attenuation to the ambient neutron and γ backgrounds and consists of, from the inside out, 5 cm of oxygen-free high-conductivity (OFHC) copper, 25 cm of boron-loaded

*Corresponding authors: muhammed.deniz@deu.edu.tr; htwong@phys.sinica.edu.tw

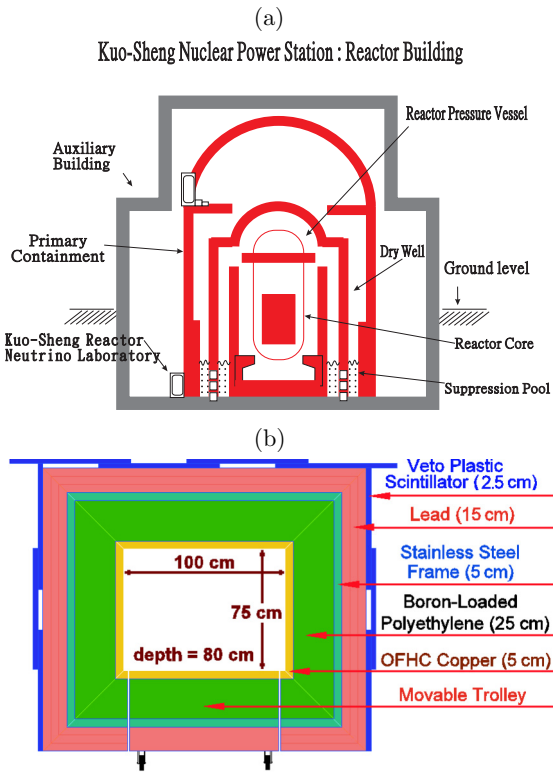

FIG. 1. (a) Schematic side view, not drawn to scale, of the Kuo-Sheng Nuclear Power Station Reactor Building, indicating the experimental site. The reactor core-detector distance is about 28 m. (b) Schematic layout of the general purpose inner-target volume, passive shielding, and cosmic-ray veto panels.

polyethylene, 5 cm of steel, 15 cm of lead, and cosmic-ray veto scintillator panels. The schematic layout of the shielding structure is shown in Fig. 1(b). Different detectors are placed in the inner volume for the different scientific programs.

The primary cosmic-ray hadronic components are greatly attenuated by matter (the nuclear interaction length of rock is about 38 cm). Their fluxes at a shallow depth of ∼30 mwe are therefore negligible. The neutron background is mostly due to (i) cosmic-ray muon-induced interactions [10] and (ii) ambient radioactivity followed by (α, n) processes from the materials in the vicinity of the detectors. The neutron fluxes and their spectra, therefore, depend on the details of the experimental hardware and shielding configurations, in addition to the depth. Neutron background measurements at shallow-depth sites have been made [11]. The typical levels for neutrons fluxes above keV are $\mathcal{O}(10^{-4}, 10^{-3}, 10^{-5})$ cm^{-2} s^{-1} for the unshielded, lead-shielded, and moderator-shielded configurations, respectively.

The KSNL shielding structures as shown in Fig. 1(b) can attenuate thermal and 1-MeV neutrons by factors of $\ll 10^{-6}$ and $\sim 10^{-4}$, respectively, according to the simulation studies. Therefore the ambient unshielded neutron fluxes are not of relevance to the physics background. Their direct measurements would be challenging due to the dominating γ background. The background neutrons are cosmic-ray induced or originate from radioactivity of hardware components in the vicinity of the detectors. The measurement of these is the theme of this work and is discussed in detail in the subsequent sections.

III. HYBRID NEUTRON DETECTOR

The design, characteristics, and performance of the HND adopted in this measurement were described in detail in our previous publication [9]. The HND is a novel detector concept initiated by this work and was custom-built for *this* particular purpose of *in situ* neutron background measurements at a localized volume at the KSNL.

The HND has unique features not provided by conventional neutron detectors. It can perform simultaneous measurement of both thermal and fast neutron fluxes, in which the neutron-induced events are identified by PSD, thereby greatly suppressing the much larger γ-ray background. The compact dimensions allow sampling of the fluxes in a relatively localized volume and under exact shielding configurations—matching well with the size [$\mathcal{O}(100)$ cm^3] of HPGe detectors. Commonly used detectors like the Bonner multisphere array spectrometer [12] would occupy too much volume to match the space constraints. Undoped liquid scintillators [13] are sensitive to fast neutrons but not thermal ones. Doped liquid scintillators are sensitive to both thermal and fast neutrons. Those with the signatures ^{6}Li$(n, \alpha)^3$H [14] or ^{10}B$(n, \alpha)^7$Li [15] can be made compact. However, the α and proton recoils that characterize thermal and fast neutrons, respectively, are not distinguishable by PSD. The thermal neutron signatures as low-energy peaks can be easily contaminated by γ background. Long-term stability of the performance of the doped scintillators may also pose technical problems. Stability has been achieved in Gd-doped liquid scintillators [16]. The high-energy (n, γ) signatures for thermal neutrons are distinctive. They have been used in low-level neutron background measurements at underground laboratories to sensitivities as low as $\mathcal{O}(10^{-9})$ cm^{-2} s^{-1}. However, capturing the γ rays would require a detector volume much larger than that allowed by this application.

The HND is constructed with two different target materials—a Bicron BC-501A liquid scintillator with a 0.113 liter cell volume and a BC-702 scintillator of thickness 0.6 cm enriched with 95% ^{6}Li as fine ZnS(Ag) phosphor powder—to be read out by a 5.1-cm-diameter photomultiplier (PMT) at the same time. A schematic drawing of the HND is shown in Fig. 2. As depicted in Fig. 3, the HND was installed at the same location as the various HPGe detectors inside the well of an NaI(Tl) anti-Compton detector and kept under the same shielding configurations and data-taking conditions. The measured ambient neutron flux is therefore the same as what the HPGe detectors were exposed to in the physics data taking.

Different particles produce different pulse shapes with the HND [9]. The normalized reference pulses of α, n_{fast}, n_{thermal}, and γ are shown in Fig. 4. In Ref. [9], two independent PSD techniques were developed, which are based on the parameter of t_{PSD}, derived from the ratio of partial (Q_p) to total (Q_t) integration of the pulses, and based on the B/A ratio of

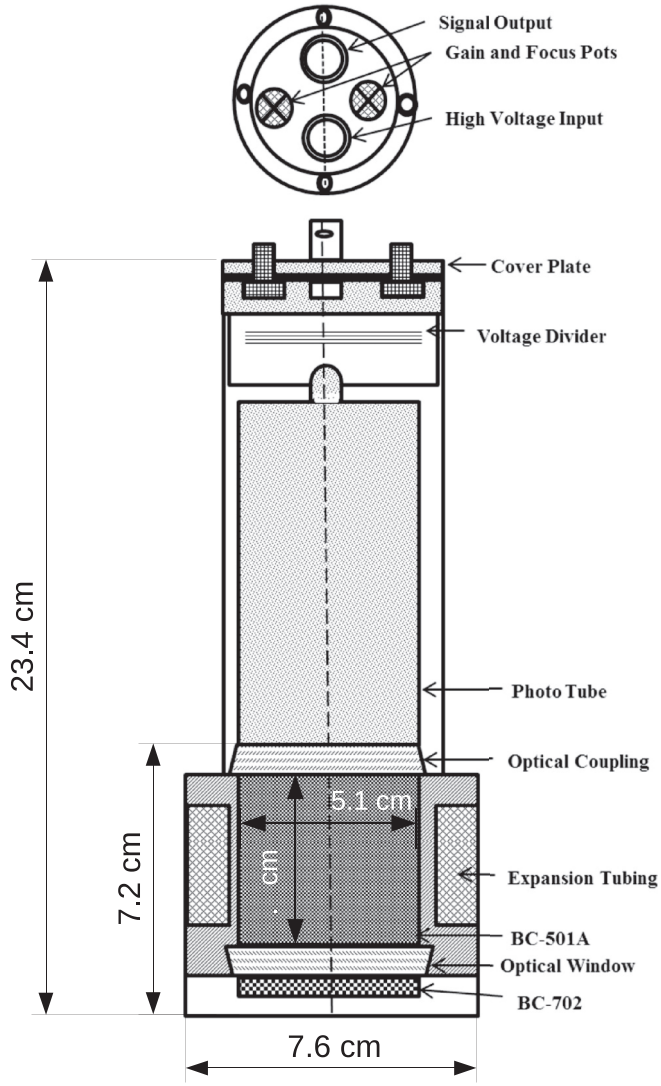

FIG. 2. Schematic diagram of the HND.

individual pulses given as

$$t_{\mathrm{PSD}} = \frac{Q_p}{Q_t} = \frac{I[(t_{20}+50\ \mathrm{ns}) : (t_{20}+150\ \mathrm{ns})]}{I[(t_{20}) : (t_{20}+150\ \mathrm{ns})]},$$
$$L = A \times (e^{-\theta(t-t_0)} - e^{-\lambda_s(t-t_0)}) + B \times (e^{-\theta(t-t_0)} - e^{-\lambda_l(t-t_0)}), \quad (1)$$

where I denotes integration of the pulse area and t_{20} represents the time where the pulses reach 20% of the amplitude. Here L represents the pulse shape, A and B are the normalization constants, t_0 is reference time, and θ, λ_s, and λ_ℓ represent decay constants. Different particles are identified by different B/A ratios for a specific scintillator.

For this study, a reference pulse is constructed by the superposition of a large number of γ-ray pulses collected from the ^{60}Co radioactive source. The parameters of the decay constants θ, λ_s, and λ_ℓ and the reference time t_0 are obtained from the fitting of the γ reference pulse. The pulse shape is

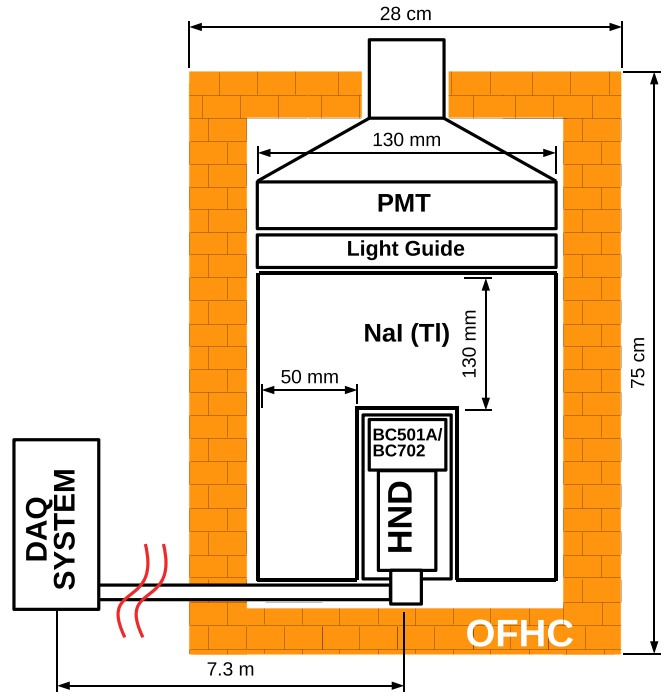

FIG. 3. Schematic view of experimental setup inside the 50-ton shielding structure (not shown). Signals are brought to the data acquisition (DAQ) system via cables of 7.3 m in length.

then parametrized as

$$L = A \times [(e^{-(t-0.52)/226.6} - e^{-(t-0.52)/17.23}) + 0.115 \times (e^{-(t-0.52)/226.6} - 1)], \quad (2)$$

where t is in nanoseconds (ns) and A is the only free normalization parameter that remains to be determined [9]. Individual pulses are fitted with the function given in Eq. (2) to identify γ against neutron events.

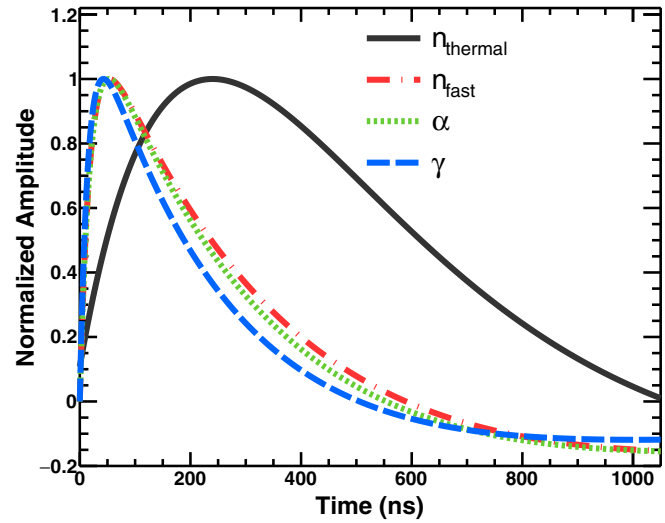

FIG. 4. Reference pulse shapes for γ-, n_{fast}-, and n_{thermal}-induced events from the HND, from which PSD techniques were devised to differentiate them. Pulse shapes of fast neutrons and α particles are very close and in practice are not distinguishable.

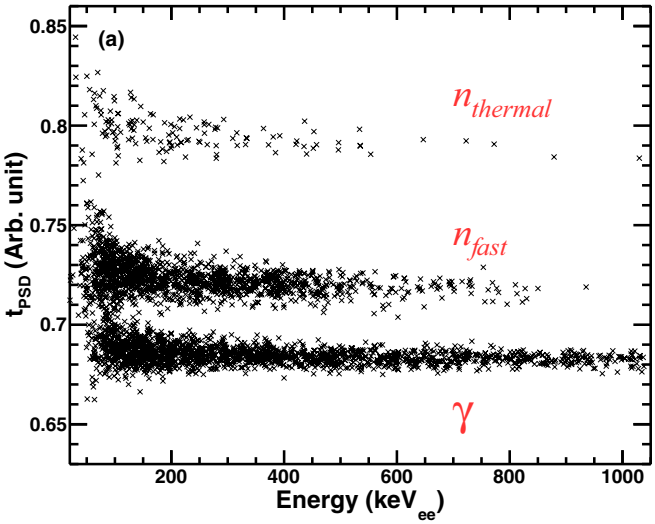

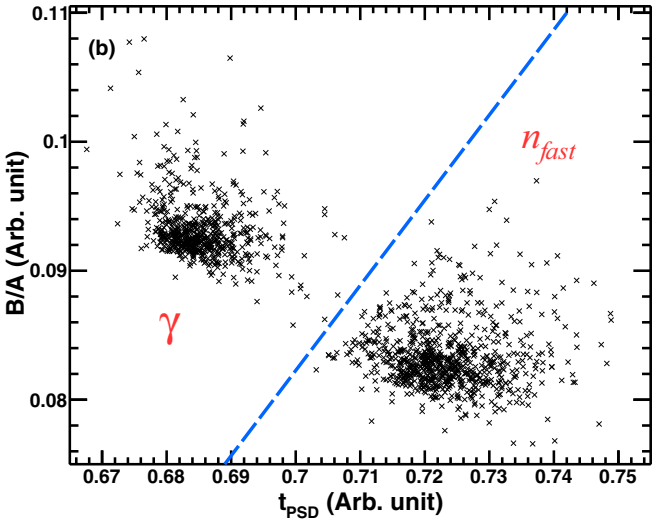

FIG. 5. PSD techniques devised to differentiate γ-, n_{fast}-, and n_{thermal}-induced events, based on (a) t_{PSD} and (b) the B/A ratio developed in Ref. [9].

The ^{241}AmBe(α, n) and ^{60}Co γ sources are used as reference for the t_{PSD} and B/A PSD techniques, respectively. Adopting the PSD parameters given in Eqs. (1) and (2), three spectral bands corresponding to γ, fast neutron, and slow neutron components of the events can be observed, as depicted in Fig. 5.

IV. DATA TAKING AT KUO-SHENG NEUTRINO LABORATORY

Several HPGe-based measurements [2,4–8] have been carried out at the KSNL. The external dimensions of the HND were selected to resemble those of HPGe detectors. Data were taken at the KSNL with the HND placed at the same location as the HPGe detector [1] under identical active and passive shielding configurations, as depicted in Fig. 3. The plastic scintillator panels function as a cosmic-ray (CR) veto detector

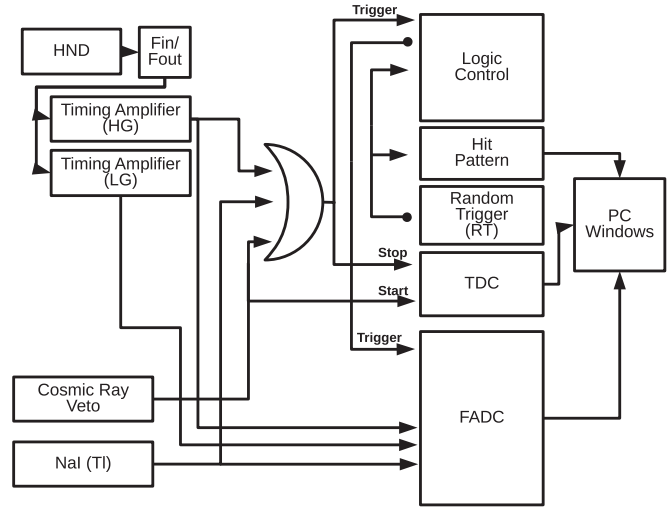

FIG. 6. Schematic block diagram of the data acquisition system.

while the well-shaped NaI(Tl) serves as an anti-Compton (AC) veto detector, and in its cavity the HND (HPGe detectors in early experiments) was placed. The HND + NaI(Tl) detectors were further shielded by OFHC copper and placed inside a sealed volume with nitrogen gas flow as a purge of the radioactive radon gas. The setup was installed inside a 50-ton shielding structure [1] consisting of, from the inside out, OFHC copper, boron-loaded polyethylene, lead, and CR panels, for suppression of ambient γ and neutron backgrounds and for tagging cosmic-ray induced events.

The schematic block diagram for the data acquisition (DAQ) system is given in Fig. 6. The HND signals higher than the discriminator threshold provide the triggers. Signals from other detector components were recorded to be used for the suppression of AC and CR events in subsequent offline analysis. The HND signals were processed by two fast-timing amplifiers [17] at different gains and recorded by 8-bit flash-analog-to-digital converters [18] at a 1-GHz sampling rate. The data-taking period lasted more than a month and a total of 33.8 live-time days of data were collected for subsequent analysis.

The goal of offline analysis is to categorize the events and determine their respective energy spectra. After standard filtering of events due to electronic noise and other spurious nonphysical triggers, the physical events are identified as γ, n_{fast}, and n_{thermal} from the reference pulse shape information as in Fig. 5. The origins of these events are derived from the AC and CR detectors according to four categories: $\text{CR}^{\pm} \otimes \text{AC}^{\pm}$ where $+(-)$ denotes coincidence (anticoincidence) of the CR or AC detector with the HND. In particular, the $\text{CR}^{+} \otimes \text{AC}^{-}$ tag selects CR neutron-induced events; the $\text{CR}^{-} \otimes \text{AC}^{+}$ tag is rich in ambient γ-induced AC events, while $\text{CR}^{-} \otimes \text{AC}^{-}$ is the condition for selecting neutrino- or WIMP-induced candidate events uncorrelated with both CR and AC systems.

V. INTERNAL CONTAMINATION OF NEUTRON DETECTOR

The measurement of the intrinsic radiopurity of the HND is essential for determining the ambient neutron background, es-

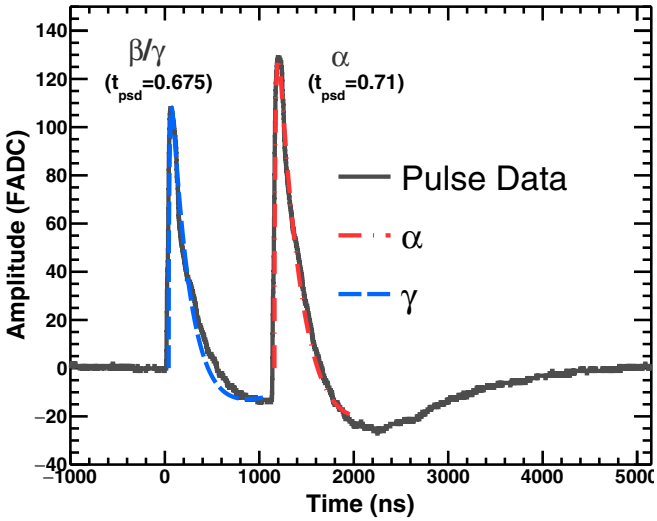

FIG. 7. A typical double-pulse event in the $CR^- \otimes AC^-$ channel.

pecially those in $CR^- \otimes AC^-$. Nuclear α decays from the ^{238}U and ^{232}Th series can mimic neutron-induced nuclear recoil signatures, and hence their contributions must be determined.

The PSD characteristics of α events as well as the unique time correlations of two decay sequences (DS) provide powerful means to measure contamination of the ^{232}Th and ^{238}U series, from which the α background can be evaluated, assuming secular equilibrium.

The related DS [19] are as follows.

(i) DS_1. Within the ^{232}Th series, there is a 64% branching ratio for ^{212}Bi to decay via a β-α cascade:

$$^{212}\mathrm{Bi} \rightarrow {}^{212}\mathrm{Po} + \bar{\nu}_e + e^- + \gamma's$$
$$(Q = 2.25\ \mathrm{MeV};\ \tau_{1/2} = 60.6\ \mathrm{min}),$$
$$^{212}\mathrm{Po} \rightarrow {}^{208}\mathrm{Pb} + \alpha(\mathrm{Q} = 8.95\ \mathrm{MeV};\ \tau_{1/2} = 0.30\ \mu\mathrm{s}).$$

(ii) DS_2. Within the ^{238}U series, there is an α-α cascade from ^{222}Rn:

$$^{222}\mathrm{Rn} \rightarrow {}^{218}\mathrm{Po} + \alpha(Q = 5.59\ \mathrm{MeV};\ \tau_{1/2} = 3.82\ \mathrm{days}),$$
$$^{218}\mathrm{Po} \rightarrow {}^{214}\mathrm{Pb} + \alpha(Q = 6.12\ \mathrm{MeV};\ \tau_{1/2} = 3.10\ \mathrm{min}).$$

A typical example of a double-pulse event is displayed in Fig. 7, interpreted as a β-α cascade based on PSD. A collection of the delayed pulses in similar cascades provides the α reference pulse shape as shown in Fig. 4. The n_{fast}/γ events are distinguishable, while n_{fast}/α events are not distinguishable on an event-by-event basis because the differences in their pulse shapes are smaller than electronic fluctuations. The α events of DS_2 are monoenergetic and well-separated in time and were used to confirm consistency with the resolution and quenching functions adopted in the analysis.

The delay-time (Δt) distributions for the correlated events from DS_1 and DS_2 are shown in Figs. 8(a) and 8(b), respectively. The results of best-fit parameters to exponential decay functions are displayed in Table I.

The measured event rate of the decay sequences of DS_1 and DS_2 can be used for the estimation of contamination

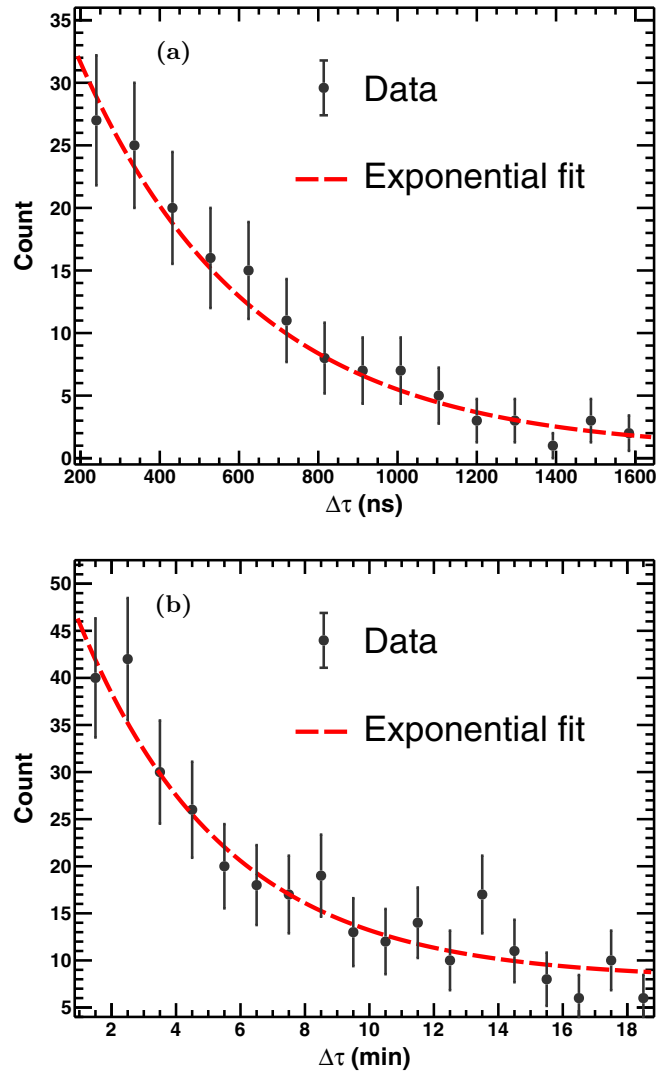

FIG. 8. Distribution for (a) β-α events from ^{212}Bi $\rightarrow$ ^{212}Po $\rightarrow$ ^{208}Pb in DS_1 and (b) α-α events from ^{222}Rn $\rightarrow$ ^{218}Po $\rightarrow$ ^{214}Pb in DS_2.

TABLE I. Summary of measured values and inferred radioactivity levels of the two cascade sequences.

Series	DS_1 ^{232}Th	DS_2 ^{238}U
Signatures	β-α	α-α
Decays	^{212}Bi $\rightarrow$ ^{212} Po $\rightarrow$ ^{208} Pb	^{222}Rn $\rightarrow$ ^{218} Po $\rightarrow$ ^{214} Pb
χ^2/n.d.f	4.7/16	9.0/17
Half-life		
Nominal	299 ns	3.10 min
Measured	302 ± 27 ns	3.14 ± 0.39 min
Counts in 33.8 days	366.20 ± 26.94	292.50 ± 15.43
Radioactivity (mBq/kg)	0.140 ± 0.010	0.110 ± 0.006
Contaminations $\times 10^{-11}$ (g/g)	2.21 ± 0.16	0.89 ± 0.048

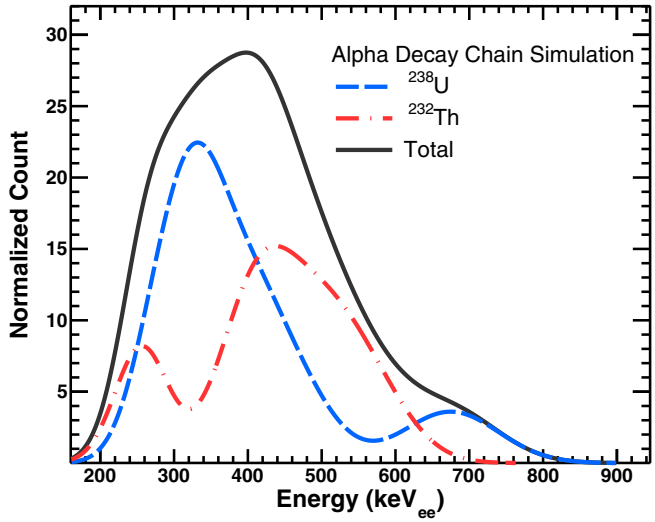

FIG. 9. Simulated α-energy spectra of ^{232}Th and ^{238}U decay chains including detector resolution and quenching effects [9]. Normalization is fixed by the measured cascade sequences of Table I.

levels of their long-lived parent isotopes of ^{232}Th and ^{238}U in the detector. Simulated α-energy spectra of the ^{232}Th and ^{238}U series, convoluted with detector resolution and quenching effects, are depicted in Fig. 9.

The measured half-lives are consistent with nominal values. The measured event rates can be translated to the radioactivity and contamination levels of their long-lived parent isotopes of ^{232}Th and ^{238}U in the detector, assuming secular equilibrium. Simulated α-energy spectra of ^{232}Th and ^{238}U parent isotopes convoluted with detector resolution and quenching effects are depicted in Fig. 9.

VI. NEUTRON BACKGROUND

A. Thermal neutron background

Thermal neutrons are those with kinetic energy below 1 eV and in thermal equilibrium with the ambient surroundings. Their energy distribution is described by the Maxwell-Boltzmann distribution with a most probable energy of $E_{\rm th} \sim 0.02$ eV, which corresponds to a velocity of $v_{\rm th} \sim 2200$ m s^{-1}.

The scintillator BC-702 used for thermal neutron measurements does not provide energy information of the incident neutron. Calculation of the thermal neutron flux is performed assuming Maxwell-Boltzmann distributions.

For a neutron flux $\phi_n(E)$ with the interaction cross section $\sigma(E)$ in the detector, the count rate in the detector is given by

$$R_{\rm th} = N \int \sigma(E)\phi_n(E)dE, \tag{3}$$

where N is the total number of target nuclei in the detector. The thermal neutron captured by ^{6}Li in the HND,

$$n + {}^6\mathrm{Li} \rightarrow {}^3\mathrm{H} + \alpha, \tag{4}$$

is inversely proportional to the neutron velocity $v(E)$, such that

$$\sigma(E) = \sigma_{\rm th}\frac{v_{\rm th}}{v(E)}, \tag{5}$$

where $\sigma_{\rm th} = 940$ b. An isotropic and homogeneous flux distribution can be described by

$$\phi(E) = v(E)\rho_n(E), \tag{6}$$

where $\rho_n(E)$ is the neutron number density at energy E in the detector volume. The count rate can therefore be expressed as

$$R_{\rm th} = N\sigma_{\rm th}v_{\rm th}\langle\rho_n\rangle, \tag{7}$$

where $\langle\rho_n\rangle$ is the energy-averaged thermal neutron number density. The average neutron velocity is given by

$$\langle v\rangle = \frac{\int v(E)\rho_n(E)dE}{\int \rho_n(E)dE} = \frac{\Phi}{\langle\rho_n\rangle}, \tag{8}$$

where Φ is the total flux. Accordingly, the rate becomes

$$R_{\rm th} = N\sigma_{\rm th}\frac{v_{\rm th}}{\langle v\rangle}\Phi. \tag{9}$$

The Maxwell-Boltzmann distribution for thermal neutrons gives rise to the relation

$$\frac{\langle v\rangle}{v_{\rm th}} = \frac{2}{\sqrt{\pi}}. \tag{10}$$

Accordingly, the total neutron flux is related to the measured count rate as

$$\Phi_n = \frac{2R_{\rm th}}{N\sigma_{\rm th}\sqrt{\pi}}. \tag{11}$$

The measured thermal neutron rate at the KSNL with the HND BC-702 is

$$R_{\rm th} = (4.15 \pm 0.12) \times 10^{-4}\ \text{counts s}^{-1}\ . \tag{12}$$

With a total number of $N = 1.41 \times 10^{22}$ ^{6}Li atoms in BC-702 [20,21], the corresponding total thermal neutron flux is

$$\Phi_n = (3.54 \pm 0.10) \times 10^{-5}\ \text{cm}^{-2}\ \text{s}^{-1}\ . \tag{13}$$

The majority of the thermal neutron events are with the $\mathrm{CR}^- \otimes \mathrm{AC}^-$ tag uncorrelated with the other detector systems, as depicted in Fig. 10. The time difference between these events with the previous CR^+ tag is displayed in Fig. 11, in which accidental coincidences from random trigger events are superimposed. An excess is observed with a correlation timescale of about 200 μs, indicating that part (20%) of thermal neutron capture events can be matched to the thermalization of specific cosmic-ray events. The timescale corresponds to that necessary for the cosmic-induced high-energy neutrons to lose their energy, get thermalized, and diffuse into the localized BC-702 volume. Similar distribution profiles have been measured and compared with simulations with gadolinium-loaded liquid scintillator at a shallow depth [22].

B. Measured nuclear recoil spectra, evaluated fast neutron flux, and projected HPGe background

Once the HND spectra are measured, unfolding algorithms as discussed in Ref. [9], followed by a Friedman smoothing algorithm [23], are applied to produce the corresponding fast neutron spectra. The expected nuclear recoil background in HPGe detectors at the same location and shielding configurations are then evaluated with full GEANT simulation [24] and

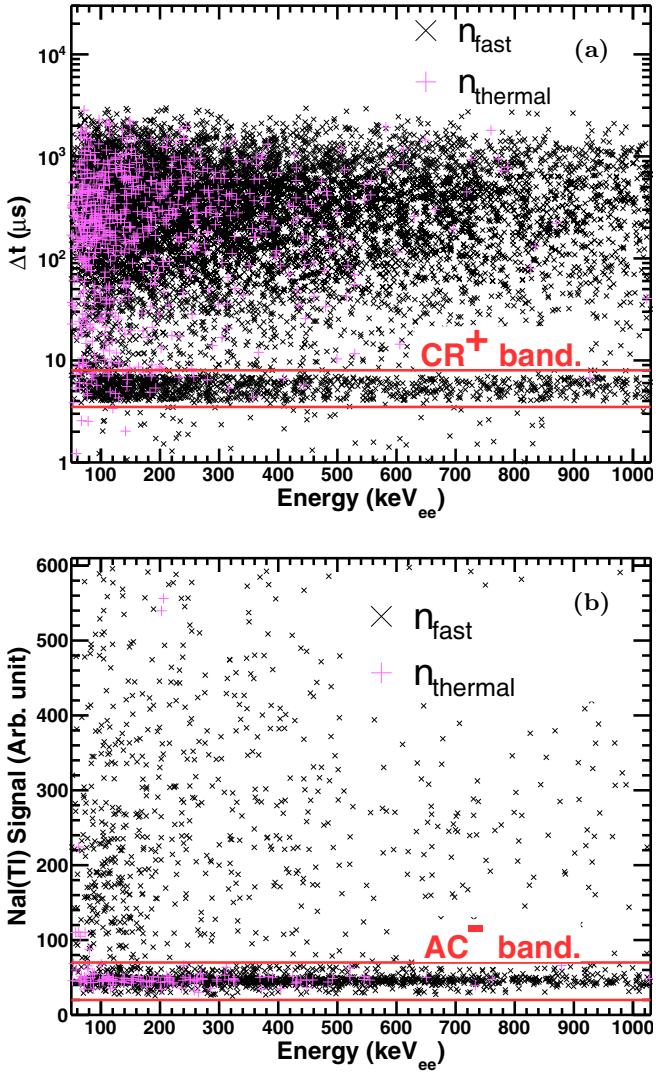

FIG. 10. Event selection criteria for (a) cosmic-ray CR^+ and (b) anti-Compton AC^- events, showing most thermal neutrons are with the $CR^- \otimes AC^-$ tag.

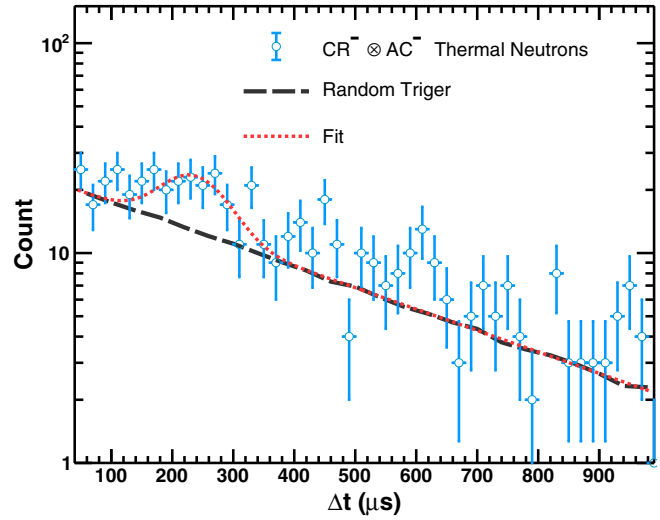

FIG. 11. The time difference between $CR^- \otimes AC^-$ thermal neutron events and the previous cosmic-ray events. Comparison with random trigger events up to ~400 μs indicates that about 20% of thermal neutrons can be matched to their parent cosmic-ray events.

compared with 173.5 kg days of data taken under identical passive and active shielding configurations with an n-type point-contact germanium detector [25]. Standard quenching functions of Ge [25] are used to convert nuclear recoil energy in keV_{nr} into the observable energy in electron-equivalence units, keV_{ee}.

Results with $CR^+ \otimes AC^-$ samples are displayed in Fig. 12, in which panel (a) is the recoil spectrum from the HND liquid scintillator, panel (b) is the evaluated neutron spectrum, and panel (c) is the projected Ge-recoil spectrum from the same neutron background. The fast neutron spectrum has a threshold at 700 keV_{nr} due to the HND response. The threshold effects give rise to a change of slope of the Ge-recoil spectrum at 4 keV_{ee}, below which the predicted spectrum is less than the measured one. This excess can be corrected for with an extrapolation to the neutron flux, the procedures and details of which are described in Sec. VI C.

The same analysis procedures are applied to the $CR^+ \otimes AC^+$ samples, and the results presented in Fig. 13 follow the same convention. There exists a finite residual spectrum after the Ge recoils are accounted for, as depicted in Fig. 13(c). The residual events are due to Compton scattering of cosmic-ray-induced high-energy ambient γ rays, characterized by a flat spectrum and consistent with simulations. The two peaks correspond to copper K_α and K_β x ray emission lines produced by the interactions of cosmic-ray muons with the copper support materials in the vicinity of the active Ge crystal.

Similarly, the results of the cosmic-ray anticoincidence samples with $CR^- \otimes AC^+$ and $CR^- \otimes AC^-$ tags are displayed in Figs. 14 and 15, respectively. It can be seen from Figs. 14(c) and 15(c) that in both cases neutron-induced Ge-recoil events, which are unrelated to cosmic-rays, only constitute a minor component relative to that due to ambient γ radioactivity. The $CR^- \otimes AC^-$ events are uncorrelated with CR and AC detectors and represent the physics candidate samples for the studies of neutrino and dark matter. The measured "recoil-like" spectrum can completely be explained by internal α contamination as discussed in Sec. V, such that only upper bounds for the HND and HPGe detectors as well as fast neutron spectra can be derived. The upper limits of these spectra at 68% C.L. are displayed in Fig. 15. The peaks in both Figs. 14(c) and 15(c) are due to x-ray emissions following electron capture (EC) by the unstable isotopes, which are produced by cosmogenic activation of long-lived isotopes inside the HPGe target.

C. Complete neutron spectrum

Combining both the measured thermal and the fast neutron fluxes and spectra, and adopting the neutron slowing-down theory [26], which is described by a $1/E$ behavior of the epithermal region in between, the complete neutron spectrum at the KSNL can be modeled using information on the *in situ* measurements of neutron capture rates.

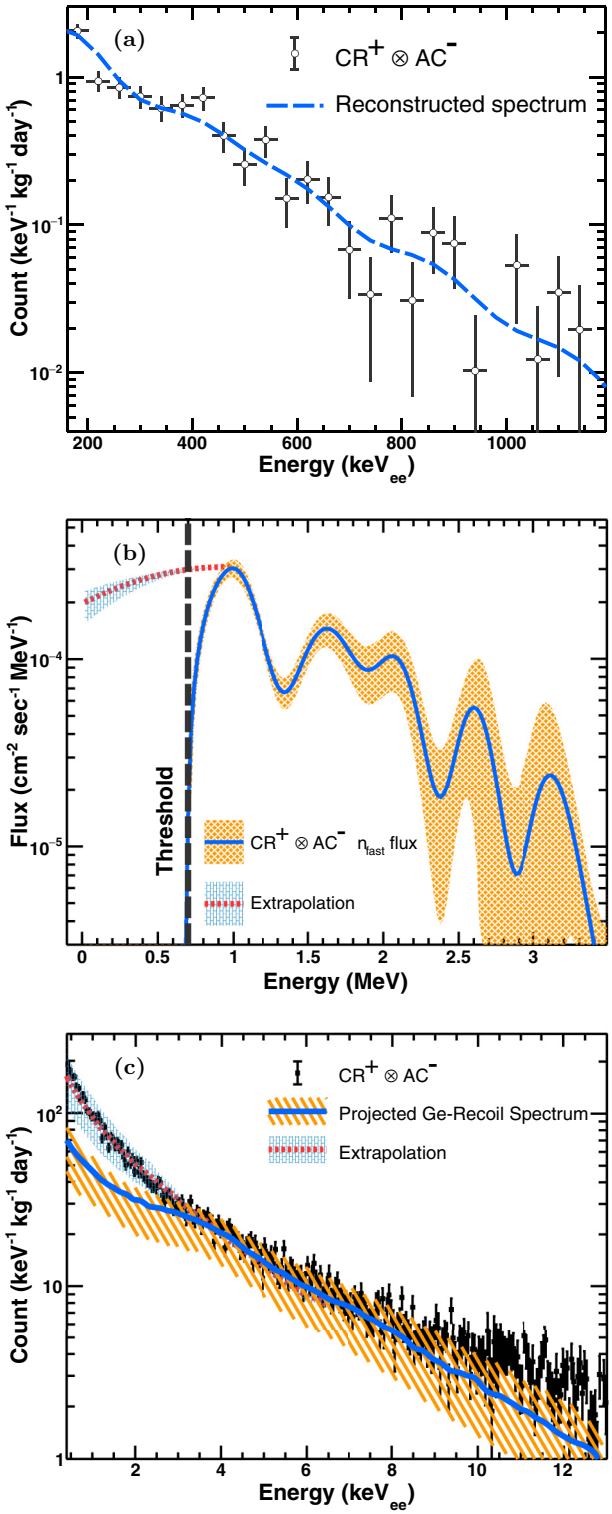

FIG. 12. Samples of $CR^+ \otimes AC^-$: (a) HND nuclear recoil energy spectrum, (b) unfolded neutron flux with $\pm 1\sigma$ error as the shadow area, and (c) the comparison of HPGe data and the predicted Ge-recoil spectrum from simulations with the measured neutron fluxes. Extrapolated spectra of panels (b) and (c) at low energy, as fixed by the neutron flux models of Fig. 17 derived from the equilibrium yield of $^{70}Ge(n,\gamma)^{71}Ge$, are corrections to the effects due to the finite HND threshold of 150 keV_{ee}.

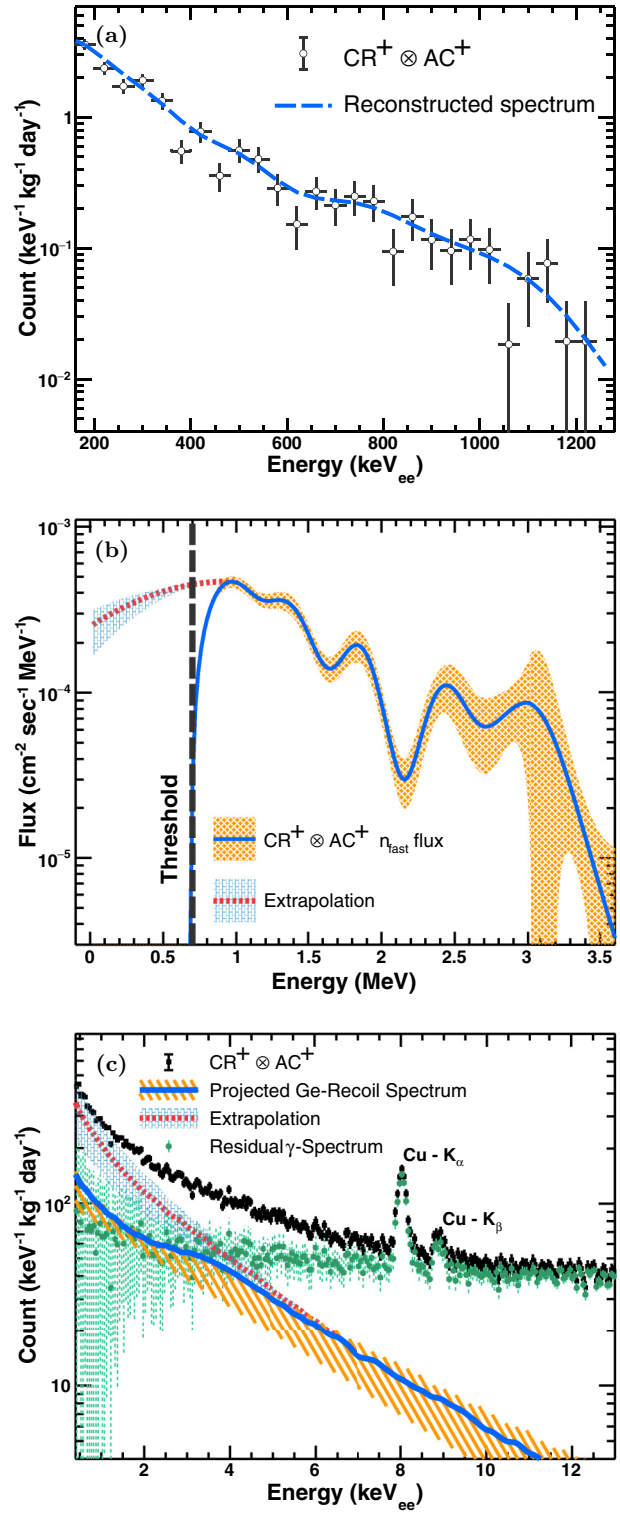

FIG. 13. Samples of $CR^+ \otimes AC^+$: (a) HND nuclear recoil energy spectrum, (b) unfolded neutron flux with $\pm 1\sigma$ error as the shadow area, and (c) the comparison of HPGe data and the predicted Ge-recoil spectrum from simulations with the measured neutron fluxes. Extrapolated spectra of panels (b) and (c) at low energy, as fixed by the neutron flux models of Fig. 17 derived from the equilibrium yield of $^{70}Ge(n,\gamma)^{71}Ge$, are corrections to the effects due to the finite HND threshold of 150 keV_{ee}.

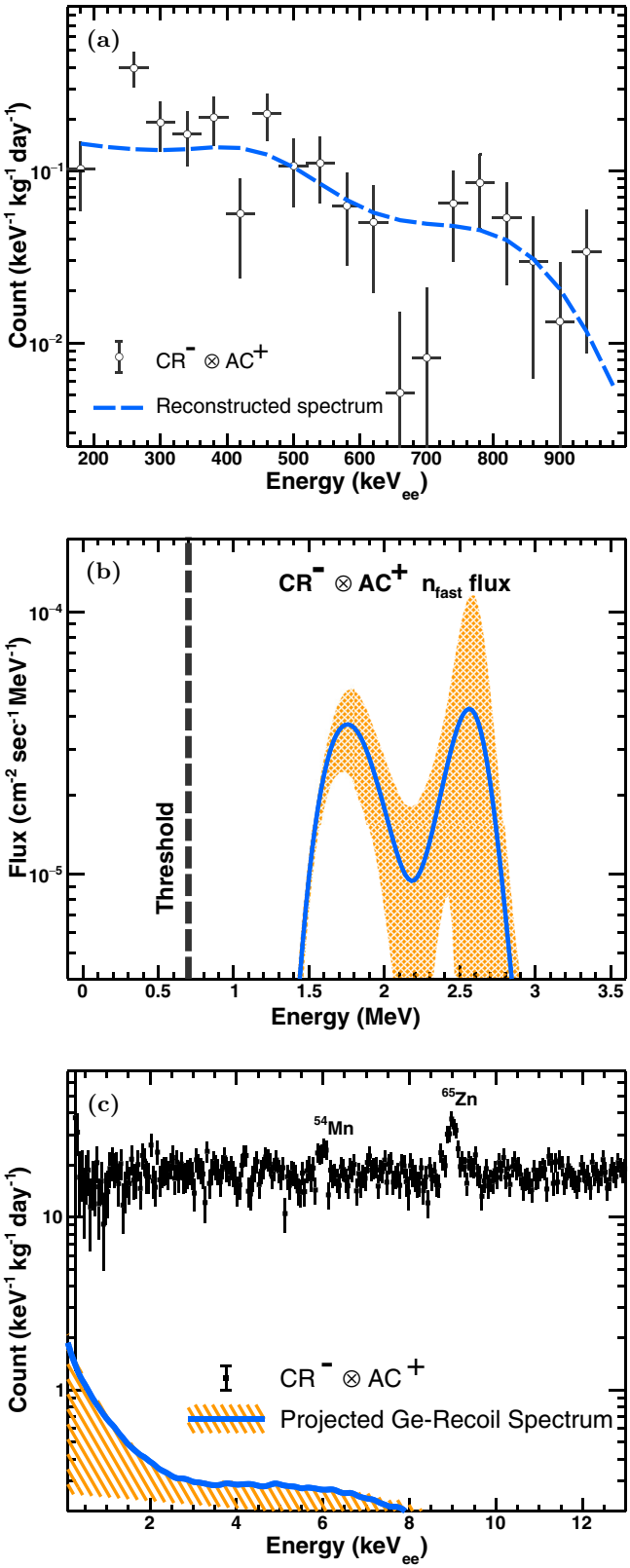

FIG. 14. Samples of $CR^- \otimes AC^+$: (a) HND nuclear recoil energy spectrum, (b) unfolded neutron flux with $\pm 1\sigma$ error as the shadow area, and (c) the comparison of HPGe data and the predicted Ge-recoil spectrum from simulations with the measured neutron fluxes.

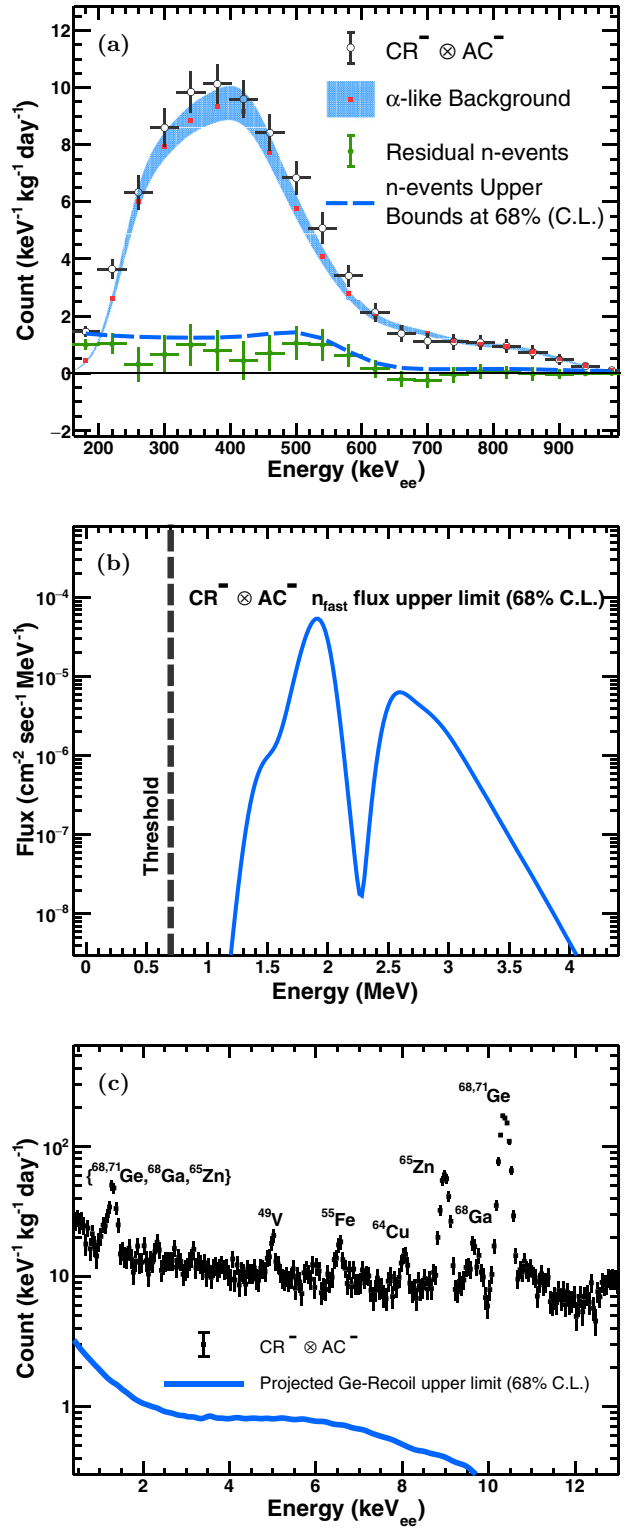

FIG. 15. Samples of $CR^- \otimes AC^-$: (a) energy spectra for HND nuclear recoil-like events, together with the measured α background from ^{232}Th and ^{238}U decay series and the 68% C.L. upper bound of neutron-induced nuclear recoils, from which the upper bounds of (b) the unfolded neutron spectrum and (c) the predicted Ge-recoil background in HPGe detectors can be derived and compared with measured data.

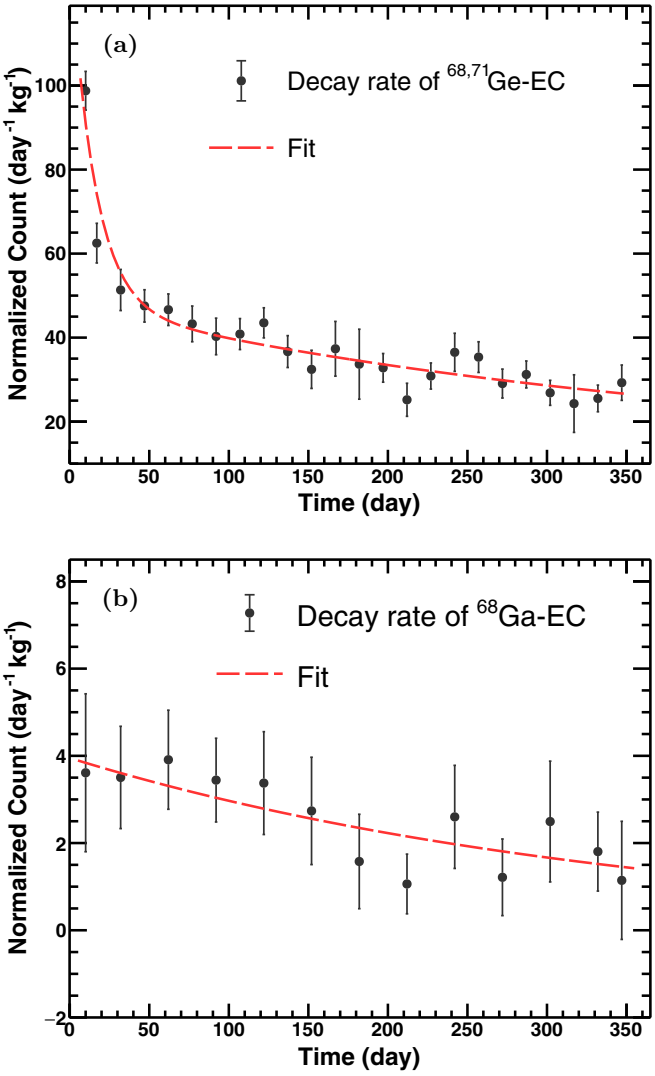

FIG. 16. Time variation of characteristic K x-ray lines of (a) ^{71}Ge and ^{68}Ge and (b) ^{68}Ga. Exponential best fits are superimposed.

Figures 16(a) and 16(b) show the variations over the whole data-taking period (347 days) of the x-ray peaks at 10.37 and 9.66 keV$_{ee}$, respectively, following EC of ^{71}Ge + ^{68}Ge and ^{68}Ga. These isotopes are primarily produced by neutron capture channels ^{70}Ge$(n,\gamma)^{71}$Ge, followed by EC in ^{71}Ge$(e^-,\nu_e)^{71}$Ga and ^{70}Ge$(n,3n)^{68}$Ge, followed by ^{68}Ge$(e^-,\nu_e)^{68}$Ga and ^{68}Ga$(e^-,\nu_e)^{68}$Zn.

The decreasing intensities with time are consequences of less *in situ* cosmogenic activation compared to the preinstallation activities. The measured lifetimes are consistent with nominal values and the equilibrium levels displayed in Table II, on the other hand, provide information on the *in situ* neutron capture rates of ^{70}Ge and hence the neutron fluxes. It can be seen from Fig. 16(b) that the equilibrium yield of the 9.66-keV$_{ee}$ line and hence *in situ* production of ^{70}Ge$(n,3n)^{68}$Ge are consistent with zero. Accordingly, the equilibrium yield of the 10.37-keV$_{ee}$ line is due exclusively to *in situ* production of ^{70}Ge$(n,\gamma)^{71}$Ge. This measured rate is used to fix the normalization of the epithermal neutron component.

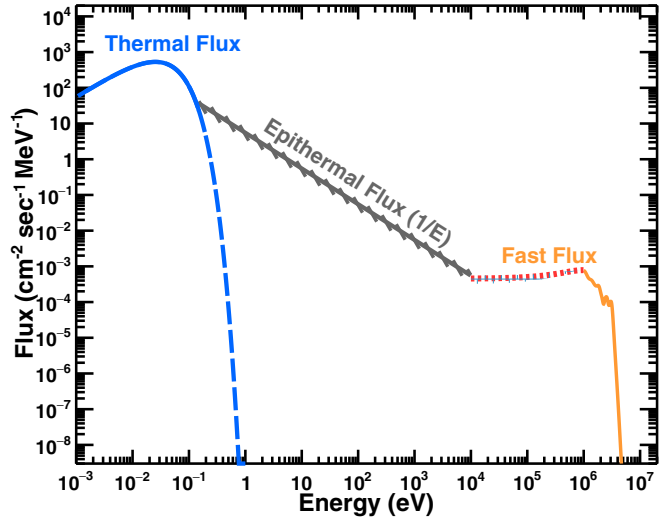

FIG. 17. Neutron spectrum model at the target region of the KSNL. The total thermal and fast neutron components are based on measurements and analysis reported in this article. The epithermal component is from interpolation. The cutoff at ∼5 MeV is a consequence of the lack of event statistics below $\mathcal{O}(10^{-2})$ kg^{-1} keV^{-1} day^{-1} above a few MeV$_{ee}$.

The complete neutron background spectrum at the KSNL is displayed in Fig. 17. The capture rates of ^{70}Ge$(n,3n)^{68}$Ge and ^{70}Ge$(n,\gamma)^{71}$Ge due to the thermal, epithermal, and fast neutron components evaluated by full GEANT simulations [24] are listed in Table II, the sum of which is in excellent agreement with the measured rates. The consistency is illustrated in the measured CR$^-$ ⊗ AC$^-$ HPGe spectra of Fig. 18 in which the different components of the Ge K x-ray lines are shown. Their total fluxes under different tags are given in Table III. The high-energy cutoff at ∼5 MeV in Fig. 17 is a consequence of the lack of event statistics below $\mathcal{O}(10^{-2})$ kg^{-1} keV^{-1} day^{-1}

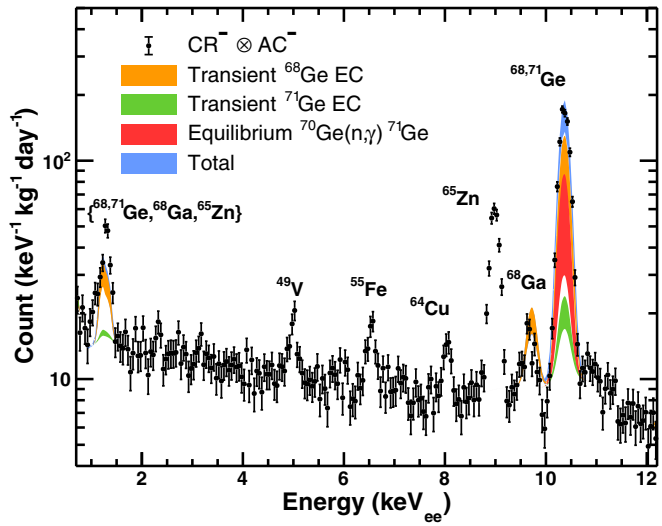

FIG. 18. Measured CR$^-$ ⊗ AC$^-$ spectrum with HPGe at the KSNL. The various contributions to the ^{71}Ge, ^{68}Ge characteristic K x-ray, L x-ray lines and the ^{68}Ga K x-ray line, based on predictions using the measured equilibrium neutron capture rates, are superimposed.

TABLE II. Summary of the *in situ* measured ^{71}Ge/^{68}Ge (10.37 keV$_{ee}$) and ^{68}Ga (9.66 keV$_{ee}$) characteristic K x-ray line rates at the KSNL—for both transient and in equilibrium components. The equilibrium yield provides information on the *in situ* neutron capture yields. The measured ^{70}Ge$(n,\gamma)^{71}$Ge rates are in excellent agreement with simulation predictions using the neutron flux model of Fig. 17 as input. The measured ^{70}Ge$(n,3n)^{68}$Ge rates are consistent with zero. There are no predictions for this channel because the threshold of ∼20 MeV is above the high-energy cutoff of Fig. 17.

Channel (K x-ray lines) measurements	Half-life ($\tau_{\frac{1}{2}}$)(day)		Rate (kg^{-1} day^{-1})
	Nominal	Measured	
^{71}Ge from transient 10.37 keV$_{ee}$	11.43	10.63 ± 1.08	2.70 ± 0.90
^{68}Ge from transient 10.37 keV$_{ee}$	270.95	275.76 ± 9.01	23.9 ± 6.4
^{68}Ge from transient 9.66 keV$_{ee}$	270.95	246.74 ± 46.16	2.2 ± 0.6
Equilibrium 9.66 keV$_{ee}$			0.05 ± 0.29
=[^{70}Ge$(n,3n)^{68}$Ge]			<0.34 (68% C.L.)
Equilibrium 10.37 keV$_{ee}$			
= [^{70}Ge$(n,\gamma)^{71}$Ge + ^{70}Ge$(n,3n)^{68}$Ge]			12.40 ± 3.70
Simulated predictions (kg^{-1} day^{-1})			^{70}Ge$(n,\gamma)^{71}$Ge
n_{thermal}			8.05 ± 0.23
$n_{\text{epithermal}}$			2.18 ± 0.67
n_{fast}			3.67 ± 1.50
Total			13.90 ± 1.65

for proton recoils at energy above a few MeV$_{ee}$. This, however, would not affect background studies and understanding of the HPGe experiments at the KSNL, because the background is dominated by the lower energy background neutron, which has much higher intensity.

Once the complete neutron background is modeled, the cutoff effects of the fast neutron spectra around 700 keV in Figs. 12(b) and 13(b) due to the HND threshold at 150 keV$_{ee}$ can be corrected by extrapolation to lower energy. The corrected Ge-recoil spectra with the additional neutrons taken into account are displayed in Figs. 12(c) and 13(c). The corrected CR$^+$ ⊗ AC$^-$ Ge-recoil spectrum provides >99% match to the measured data, confirming the expected physical picture where CR$^+$ ⊗ AC$^-$ samples are dominated by nuclear recoil events due to interactions of cosmic-ray-induced fast neutrons. Similarly, the corrected CR$^+$ ⊗ AC$^+$ Ge-recoil spectrum has the expected exponential decrease with energy. Once accounted for, the residual cosmic-induced γ background is flat down to sub-keV, also expected from Compton scattering of high-energy γ rays. The consistencies of these independent measurements serve as nontrivial cross-checks on the validity of neutron flux measurements as well as on the experimental approaches and analysis procedures reported in this work.

TABLE III. Summary of flux measurements of different categories of neutrons.

Neutrons	Measured fluxes Φ_n (cm^{-2} s^{-1})
Thermal: 0.02–1.00 eV	
CR$^+$ ⊗ AC$^-$	$(2.68 \pm 0.28) \times 10^{-6}$
CR$^+$ ⊗ AC$^+$	$(3.00 \pm 0.29) \times 10^{-6}$
CR$^-$ ⊗ AC$^+$	$(9.33 \pm 1.65) \times 10^{-7}$
CR$^-$ ⊗ AC$^-$	$(2.87 \pm 0.09) \times 10^{-5}$
Epithermal	$>4.39 \times 10^{-5}$ $<8.25 \times 10^{-5}$
Fast: 0.70–4.00 MeV	
CR$^+$ ⊗ AC$^-$	$(2.35 \pm 1.60) \times 10^{-4}$
CR$^+$ ⊗ AC$^+$	$(4.53 \pm 2.29) \times 10^{-4}$
CR$^-$ ⊗ AC$^+$	$(1.49 \pm 5.75) \times 10^{-6}$
CR$^-$ ⊗ AC$^-$	$<3.22 \times 10^{-6}$

VII. SUMMARY AND PROSPECTS

We report in this article *in situ* measurements of neutron-induced background at the KSNL with a HND under identical active and passive shielding configurations during the neutrino physics measurements. The different components of neutron fluxes thus derived are summarized in Table III, and the neutron spectrum is depicted in Fig. 17. The derived neutron spectrum provides excellent agreement with the cosmic-ray neutron-induced Ge-recoil spectra as shown in Figs. 12(c) and 13(c), thereby providing strong support to the validity of the results as well as the experimental approaches and analysis procedures.

It was demonstrated that elastic nuclear recoil events due to cosmic-ray-induced high-energy neutrons contribute almost exclusively to the CR$^+$ ⊗ AC$^-$ channel below 12 keV$_{ee}$ and are major components of the CR$^+$ ⊗ AC$^+$ channel, dominating over γ-induced background below 4 keV$_{ee}$. On the other hand, contributions of cosmic-uncorrelated neutrons to the background are minor in CR$^-$ ⊗ AC$^+$ and unobservable in CR$^-$ ⊗ AC$^-$. In particular, the dominant background to the studies of neutrinos, WIMP dark matter, and axions with CR$^-$ ⊗ AC$^-$ selection at the KSNL are ambient γ radioactivity and intrinsic cosmogenic activation. Contributions of neutrons from ambient radioactivity and reactor operation are negligible, a feature consistent with expectations from full GEANT simulations. The HND detector concept and analysis procedures can be applicable to characterizing neutron background in other rare-event experiments, in both surface and underground laboratories. In particular, the equilibrium levels of the x-ray peaks in HPGe detectors can be used to

measure *in situ* background neutron fluxes. This technique can be extended to other Ge-based underground WIMP-search experiments [27–29].

ACKNOWLEDGMENTS

This work is supported by Contract No. 114F374 under Scientific and Technological Research Council of Turkey (TUBITAK), the Academia Sinica Principal Investigator Award, Contract No. 104-2112-M-001-038-MY3 from the Ministry of Science and Technology, and Taiwan and Contract No. 2017-ECP2 from the National Center of Theoretical Sciences, Taiwan. M.K.S. thanks the University Grants Commission (UGC), Government of India, for the funding through the UGC D.S. Kothari Postdoctoral Fellowship (DSKPDF) scheme (Grant No. F. 4- 2/2006 (BSR)/PH/15-16/0098).

[1] H. T.-K. Wong, The Universe **3** 22 (2015).
[2] H. B. Li *et al.*, Phys. Rev. Lett. **90**, 131802 (2003); H. T. Wong *et al.*, Phys. Rev. D. **75**, 012001 (2007).
[3] M. Deniz *et al.*, Phys. Rev. D **81**, 072001 (2010).
[4] J. W. Chen, H. C. Chi, H. B. Li, C. P. Liu, L. Singh, H. T. Wong, C. L. Wu, and C. P. Wu, Phys. Rev. D **90**, 011301(R) (2014).
[5] H. T. Wong *et al.*, J. Phys.: Conf. Ser. **39**, 266 (2006); S. Kerman, V. Sharma, M. Deniz, H. T. Wong, J.-W. Chen, H. B. Li, S. T. Lin, C.-P. Liu, and Q. Yue (TEXONO Collaboration), Phys. Rev. D **93**, 113006 (2016).
[6] S. T. Lin *et al.*, Phys. Rev. D **79**, 061101(R) (2009); H. B. Li *et al.*, Phys. Rev. Lett. **110**, 261301 (2013).
[7] H. M. Chang *et al.*, Phys. Rev. D **75**, 052004 (2007).
[8] M. Deniz *et al.*, Phys. Rev. D **82**, 033004 (2010); S. Bilmis *et al.*, *ibid.* **85**, 073011 (2012); S. Bilmis, I. Turan, T. M. Aliev, M. Deniz, L. Singh, and H. T. Wong, *ibid.* **92**, 033009 (2015); M. Deniz, B. Sevda, S. Kerman, A. Ajjaq, L. Singh, H. T. Wong, and M. Zeyrek, *ibid.* **95**, 033008 (2017); B. Sevda *et al.*, *ibid.* **96**, 035017 (2017).
[9] M. K. Singh *et al.*, Nucl. Instrum. Methods Phys. Res., Sect. A **868**, 109 (2017).
[10] D. M. Mei and A. Hime, Phys. Rev. D **73**, 053004 (2006).
[11] A. Da Silva *et al.*, Nucl. Instrum. Methods Phys. Res., Sect. A **354**, 553 (1995).
[12] M. Awschalom and R. S. Sanna, Radiat. Prot. Dosim. **10**, 89 (1985).
[13] C. Zhang *et al.*, Nucl. Instrum. Methods Phys. Res., Sect. A **729**, 138 (2013).
[14] C. D. Bass *et al.*, Appl. Radiat. Isot. **77**, 130 (2013).
[15] S. C. Wang *et al.*, Nucl. Instrum. Methods Phys. Res., Sect. A **432**, 111 (1999).
[16] Q. Du *et al.*, Nucl. Instrum. Methods Phys. Res., Sect. A **889**, 105 (2018), and references therein.
[17] Canberra 2111 timing amplifier, data sheet available at http://phy.fiu.edu/pub/TWiki/MAST_Diagnostic/Equipment_Amplifier.pdf.
[18] National Instruments, PXI-5154 FADC, data sheet available at http://www.ni.com/pdf/manuals/376291b.pdf.
[19] S. Y. F. Chu, L. P. Ekstrom, and R. B. Firestone, The Lund/LBNL Nuclear Data Search, http://nucleardata.nuclear.lu.se/toi/.
[20] J. B. Birks, *The Theory and Practice of Scintillation Counting* (Pergamon, Elmsford, NY, 1964).
[21] BC-702 data sheet available at https://www.crystals.saint-gobain.com/sites/imdf.crystals.com/files/documents/sgc-bc702-data-sheet_70148.pdf; BC501-A data sheet available at https://www.crystals.saint-gobain.com/sites/imdf.crystals.com/files/documents/sgc-bc501-501a-519-data-sheet_69711.pdf.
[22] Q. Du *et al.*, Astropart. Phys. **102**, 12 (2018).
[23] J. H. Friedman, California LCS Technical Report No. 5 SLAC PUB-3477, 1974.
[24] GEANT4 Collaboration - S. Agostinelli *et al.*, Nucl. Instr. and Meth. A **506**, 250-303, SLAC-PUB-9350 (2003), FERMILAB-PUB-03-339.
[25] A. K. Soma *et al.*, Nucl. Instrum. Meth. Phys. Res., Sect. A **836**, 67 (2016).
[26] Y. Oka, Editor, *Nuclear Reactor Design* (Springer, New York, 2010), p. 52; J. R. Lamarsh, *Introduction to Nuclear Reactor Theory* (Addison–Wesley, Reading, MA 1966).
[27] C. E. Aalseth, *et al.*, Phys. Rev. D **88**, 012002 (2013).
[28] L. T. Yang *et al.*, Chin. Phys. C **42**, 23002 (2018); H. Jiang *et al.*, Phys. Rev. Lett. **120**, 241301 (2018).
[29] R. Agnese *et al.*, Phys. Rev. D **97**, 022002 (2018); Phys. Rev. Lett. **120**, 061802 (2018).